Available online at www.sciencedirect.com
ScienceDirect
Journal of Computational Physics 227 (2008) 7346–7367
JOURNAL OF COMPUTATIONAL PHYSICS
www.elsevier.com/locate/jcp

An efficient front-tracking method for fully nonlinear interfacial waves

Fan Ping *

Institute of Mechanics, Chinese Academy of Sciences, No. 15 Beisihuanxi Road, Beijing 100190, China

Received 11 September 2007; received in revised form 21 April 2008; accepted 22 April 2008
Available online 6 May 2008

Abstract

A fully nonlinear and dispersive model within the framework of potential theory is developed for interfacial (2-layer) waves. To circumvent the difficulties arisen from the moving boundary problem a viable technique based on the mixed Eulerian and Lagrangian concept is proposed: the computing area is partitioned by a moving mesh system which adjusts its location vertically to conform to the shape of the moving boundaries but keeps frozen in the horizontal direction. Accordingly, a modified dynamic condition is required to properly compute the boundary potentials. To demonstrate the effectiveness of the current method, two important problems for the interfacial wave dynamics, the generation and evolution processes, are investigated. Firstly, analytical solutions for the interfacial wave generations by the interaction between the barotropic tide and topography are derived and compared favorably with the numerical results. Furthermore, simulations are performed for the nonlinear interfacial wave evolutions at various water depth ratios and satisfactory agreement is achieved with the existing asymptotical theories.

Keywords: Moving boundary; Front-tracking; Nonlinear interfacial waves; KdV theory

1. Introduction

It is well known that in computation of free surface (interface) flows accurate modeling of the moving boundary is an extremely challenging problem in CFD as the position of the moving boundary at a given time is unknown *a priori* and must be calculated as part of the solution. To alleviate the involved computational burden, two distinct techniques are proposed for approximating the moving boundary: *front capturing* and *front-tracking*.

The 'front-capturing' technique is based on fixed spatial domains and characterized by treating the interface as a high variation region with no explicit elements to represent the interface. Examples of this technique including the 'volume-of-fluid' method [1] and the 'level-set' method [2], both use an auxiliary scalar field, which is updated by solving a scalar transport equation, to determine the location of the interface. With these

* Tel.: +86 10 82544205; fax: +86 10 62561284.
E-mail address: fanping@imech.ac.cn

0021-9991/$ - see front matter © 2008 Elsevier Inc. All rights reserved.
doi:10.1016/j.jcp.2008.04.021

methods it is easier to model complex flow phenomena such as cavitation and wave breaking without requiring fundamental changes to their algorithm. However, a major disadvantage of these methods is undisputed that the interface diffusion over several cells can result in loss of precision.

By contrast, the 'front-tracking' method [3–5] generally treats the surface (interface) as a linked set of point forming an unstructured mesh which moves through a stagger Eulerian grid and deforms as the simulation advances in time. This strategy has a significant advantage: the surface profile preserves its nature as a well-defined delineated interface without any smearing of its profile, which ensures the 'front-tracking' approach more accurate than the 'front-capturing' technique. However, to account for topological changes in the interface, the implementation usually becomes more complex such that additional computational resources are required. Recently, the 'front-capturing' and 'front-tracking' techniques for finite element computations are also developed successfully [6,7], nevertheless, implementations for the mesh algorithm and computational process remain still quite burdensome.

Within the framework of potential theory, this study attempts to provide a novel and efficient technique to track the moving boundaries with less effort. Essential parts of the numerical method are: application of the Green's theorem to solve the Laplace equation, use of the dynamic boundary condition to evaluate the boundary potentials, and application of the total time derivative to account for the displacements of the moving boundaries. More importantly, it is worthwhile noting that the material derivatives of potentials on the moving boundaries are irrespective of the horizontal spatial differentiations. This is ensured by the fundamental characteristic of the meshes which are fixed horizontally but move freely in the vertical direction. In order to validate the efficiency of this method, analytical solutions for the nonlinear interfacial waves are used to compare with the numerical results. As a consequence, it is helpful in the ensuing part to give a brief review on the separate applicability and limitation of the existing asymptotical theories.

The KdV-type models have been widely used for the investigation of nonlinear internal waves and play the primary role in elucidating the essential features of internal solitary waves [8–11]. However, the often observed broadening of the wave shapes can not be described by this kind of equations unless the extended KdV (eKdV) equation is adopted, which includes cubic nonlinearity and has been applied efficiently for the wave evolution where effects of the cubic nonlinearity dominate that of the quadratic nonlinearity [12,13]. Because of the inclusion of higher nonlinearity, the eKdV model is able to capture wave shapes of the 'thick' solitary waves as a maximum wave amplitude $A_{0\max} = -\alpha_1/\alpha_2$ is reached (α_1 and α_2 denote the quadratic and cubic nonlinearity, and the expressions can be found in Section 4.2) [14]. In general, these models are restricted to weakly nonlinear problem, and the oceanic observations of large amplitude waves (relative to the water depth) necessitate finite amplitude theories to accurately elucidate the wave properties of strong nonlinearity.

An important two-layer model extending to the weakly nonlinear eKdV theory was newly derived by Choi and Camassa (CC) [15], which permits strong nonlinearity but uses weak dispersion approximation. Evolution equations equivalent to the CC model were formulated by Ostrovsky and Grue [16] for strongly nonlinear dispersive waves. In the rigid-lid Boussinesq limit, the strongly nonlinear theories produce a maximum wave with amplitude $A_{0\max} = (h_1 - h_2)/2$ (h_1 and h_2 are the two-layer thickness) which reaches mid-depth and has a tendency of infinite wavelength [15,16]. It is found that the aforementioned weakly (eKdV) and strongly nonlinear (CC) theories agree quite well for $0.4 < h_1/h_2 < 0.6$, while, differences become remarkable outside this range [14]. Particularly, for a critical problem ($h_1/h_2 = 1$ in Boussinesq approximation), both the weakly and strongly nonlinear theories have suggested that the maximum wave amplitude for the solitary wave solutions vanishes, namely, no steady solitary wave solution exists in this situation. In general, the asymptotic models have limited applications not only at the critical depth ratio but also at the non-critical depth ratio if solitary waves of sufficient amplitudes are considered [17].

The above mentioned limitations of the analytical methods motivate us to construct a fully nonlinear and dispersive model for scrutinizing behaviors of strongly nonlinear interfacial waves at various depth ratios. Two important processes for the interfacial wave dynamics are investigated to validate the reliability of this numerical method. First, for the interfacial wave generations by the interaction between the barotropic tide and topography, the simulations are compared well with the analytical solutions. Then, this model is applied for the interfacial wave evolutions. Weakly and strongly nonlinear interfacial solitary waves are recomputed at the non-critical depth ratios, arriving at the results described by the asymptotical theories. Finally, special

attentions are directed to the transient processes of nonlinear interfacial waves at the critical depth ratio and the wave properties in such a unique situation are studied preliminarily.

2. Mathematical model

This study considers two-dimensional motions of two fluid layers under the Boussinesq approximation. The upper fluid layer has thickness h_1 at rest and constant density ρ_1, and the lower layer has undisturbed thickness h_2 and constant density ρ_2, where ρ_1 is smaller than ρ_2. The relative density difference between the two-layers is $\sigma = (\rho_2 - \rho_1)/\rho_2$ (the Boussinesq approximation ensures $\sigma << 1$). The topography is characterized by $H(x)$ with a maximum H_0. A schematic view of the problem is shown in Fig. 1. It is assumed that the two fluids are homogeneous and incompressible and that the motion in each of the layers is irrotational such that the potential theory can be applied. Therefore, the equation governing the flow is Laplace's equation for the velocity potential, ϕ, i.e.

$$\Delta\phi = 0 \tag{1}$$

At the free surface two boundary conditions must be satisfied. The first is the kinematic condition,

$$\frac{\partial\eta}{\partial t} = \frac{\partial\phi}{\partial z} - \frac{\partial\eta}{\partial x}\frac{\partial\phi}{\partial x} \tag{2}$$

where η is the surface elevation. The second is the dynamic condition,

$$\frac{\partial\phi}{\partial t} + \frac{1}{2}\left[\left(\frac{\partial\phi}{\partial x}\right)^2 + \left(\frac{\partial\phi}{\partial z}\right)^2\right] + g\eta = 0 \tag{3}$$

where g is the acceleration due to gravity. At the interface, the kinematic boundary condition is similar as that at the surface, written as,

$$\frac{\partial\zeta}{\partial t} = \frac{\partial\phi_i}{\partial z} - \frac{\partial\zeta}{\partial x}\frac{\partial\phi_i}{\partial x}, \quad i = 1, \text{or, } 2 \tag{4}$$

where ζ denotes the interface elevation. The subscripts 1 and 2 represent the upper and lower layers, respectively. In addition to the above kinematic condition, the continuity condition for the normal velocity across the interface is also required,

$$\frac{\partial\phi_1}{\partial\mathbf{n}} = \frac{\partial\phi_2}{\partial\mathbf{n}} = V_{\mathbf{n}} \tag{5}$$

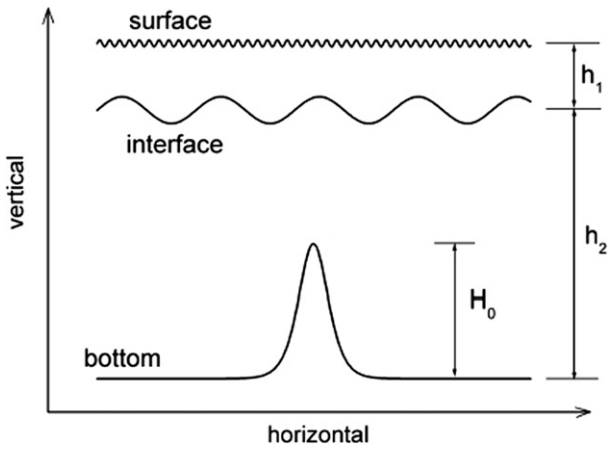

Fig. 1. Sketch for a two-layer system. h_1 (h_2): the undisturbed thickness of the upper (lower) layer;H_0: the maximum height of the bottom.

where **n** is the direction normal to the interface, $V_{\mathbf{n}}$ is the normal velocity of the interface along **n**. The dynamic boundary condition at the interface is obtained by balancing the pressure,

$$p_1 = p_2 \tag{6}$$

and the pressure is given by the Bernoulli equation, i.e.

$$\frac{p_i}{\rho_i} + \frac{\partial \phi_i}{\partial t} + \frac{1}{2}\left[\left(\frac{\partial \phi_i}{\partial x}\right)^2 + \left(\frac{\partial \phi_i}{\partial z}\right)^2\right] + g\zeta = 0, \quad i = 1, 2 \tag{7}$$

In consideration of the internal tide generation, the bottom boundary condition reads,

$$\frac{\partial \phi}{\partial z} = U\frac{\partial H}{\partial x} \tag{8}$$

where U is the horizontal component of the tidal current velocity on the bottom surface. For a flat floor, the term on the RHS of the above equation becomes zero.

3. Numerical method

Usually, when performing a wave simulation one may encounter significant difficulties arisen from the moving boundary problem. As mentioned in Section 1, a tractable 'interface-tracking' technique based on the mixed Eulerian and Lagrangian concept is employed to circumvent this problem. Before detailing the numerical method, it is necessary to highlight the pivotal idea in advance.

The computing domain is partitioned homogeneously into structured quadrangular meshes suitable for the boundary configuration, as sketched in Fig. 2. When the surface and interface move to new positions, the whole area needs to be re-grided, but the total number of the grids keeps unchanged. The fact that the vertical scale of each grid varies along with the departures of the free boundaries prompts us to apply the Lagrangian method to calculate the potentials at the boundaries. That is to say, when the dynamic boundary condition is used to evaluate the potentials, the total time derivative should be applied to account for the movements of the boundaries. Importantly, an essence should be emphasized that the horizontal scale of each cell does not change during the whole computing period. This is in line with the Eulerian concept and leads to an absence of the horizontal spatial differentiations in the material derivatives for the potentials in each Lagrangian time interval. As a consequence, a modified dynamic boundary condition is required to evaluate the boundary potentials.

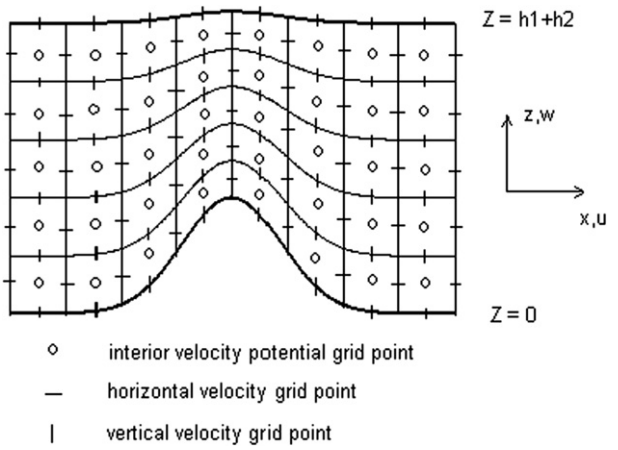

Fig. 2. A schematic illustration of the computational grids showing the interior velocity potential vector points and the velocity points.

3.1. Discretization for the governing equation

In the whole domain, the potential variable, ϕ, is defined exclusively at the geometric center of each unit. More specifically, for the inner structured grid, ϕ is defined at the cell's center, while, for the boundary unit, this unknown variable is specified at the midpoint of each segment. By applying the Green's theorem, the integral of the governing equation can be transformed into a contour integral,

$$\int\int_{\Omega_i} \Delta\phi \, d\mathbf{\Omega} = \oint_{\partial\Omega_i} \left(\frac{\partial \phi}{\partial x} dz - \frac{\partial \phi}{\partial z} dx \right) = 0 \tag{9}$$

here $\mathbf{\Omega}$ and $\partial\Omega_i$ denote the area and boundary of a unit cell, Ω_i. In keeping with the concept of the finite volume method, the discretization of the governing equation for an interior cell unit (i,j) (see Fig. 3) can be written as,

$$\left(\frac{\phi_{i+1,j} - \phi_{i,j}}{\Delta x} \cos^2 \chi^n_{i+} + \frac{\phi_{i-1,j} - \phi_{i,j}}{\Delta x} \cos^2 \chi^n_{i-} \right) \Delta z^n_i + \left(\frac{\phi_{i,j+1} - \phi_{i,j}}{\Delta z^n_i} + \frac{\phi_{i,j-1} - \phi_{i,j}}{\Delta z^n_i} \right) \Delta x = 0 \tag{10}$$

where Δx and Δz^n_i represent the grid spacing in the x and z directions, respectively; the superscript n denotes the time step; symbol $\chi^n_{i\pm}$ describes the angle between the local and orthogonal coordinates at the left and right sides of the cell center,

$$\cos \chi^n_{i\pm} = \frac{\Delta x}{\sqrt{\Delta x^2 + \left(z^n_{i\pm1,j} - z^n_{i,j} \right)^2}} \tag{11}$$

where $z^n_{i,j}$ denotes the vertical coordinate of the cell (i,j)'s center. Apparently, equations (9) and (10) do not contain the time variable, indicating all of the potentials in the interior should be calculated simultaneously in each time interval through solving a large sparse matrix with the known and time-dependent boundary potentials served as coefficients of the matrix. After all of the interior potential variables (including those on the two sides of interface) are determined, the boundary potentials as well as the displacements of the moving boundaries can thus be evaluated by using the kinematic and modified dynamic conditions.

3.2. Tracking the moving boundaries

Usually, to calculate the displacement of free surface, the most direct approach is to make use of the kinematic condition. Fig. 4 sketches the movement of the free surface, $z=\eta(t)$, from time $t = t_0$ to t_1. During this time interval a surface particle initiated at $x = x_0$ is assumed moving from $z_0 = \eta(x_0, t_0)$ to $z_2 = \eta(x_1, t_1)$. The

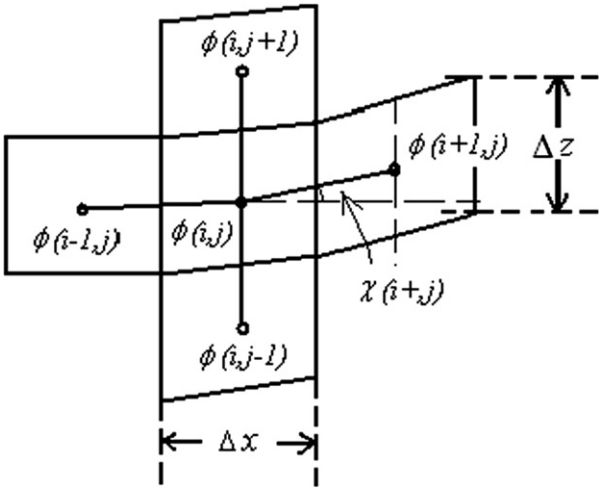

Fig. 3. Discretization of an interior cell (i,j).

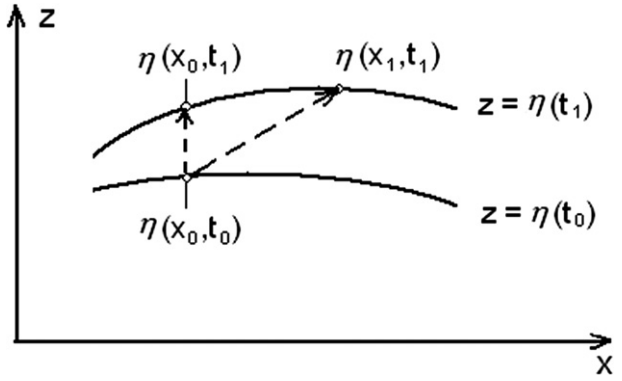

Fig. 4. A schematic drawing for the movement of the surface in the time interval (t_0, t_1).

position $z_1 = \eta(x_0, t_1)$ denotes the height of surface $\eta(t_1)$ at the coordinate $x = x_0$. By bearing the basic feature of this model in mind that the moving mesh system is fixed horizontally, we are motivated to bridge a relation between $z_0 = \eta(x_0, t_0)$ and $z_1 = \eta(x_0, t_1)$, which can be readily derived from the kinematic condition,

$$\eta(x_0, t_1) = \eta(x_0, t_0) + \Delta t \left\{ \left[\frac{\partial \phi}{\partial z}\right]_{z_0} - \left[\frac{\partial \eta}{\partial x}\frac{\partial \phi}{\partial x}\right]_{z_0} \right\} \tag{12}$$

where subscript z_0 denotes the quantities at the location $z_0 = \eta(x_0, t_0)$. On the other hand, the above relation can be constructed as well from the geometrical relationship between the three points depicted in Fig. 4. It is not difficult to identify from Fig. 4 the following equalities:

$$\begin{aligned} z_2 - z_0 &= \frac{\partial \phi}{\partial z}\Delta t, \\ z_2 - z_1 &= \frac{z_2 - z_1}{\Delta x}\frac{\Delta x}{\Delta t}\Delta t = \frac{\partial \eta}{\partial x}\frac{\partial \phi}{\partial x}\Delta t \end{aligned} \tag{13}$$

The above first equation means that the variation of vertical coordinates of a free surface particle equals the product of the vertical velocity and time interval. This is in accordance with the Lagrangian description of the movement of a particle. The latter one is easily understandable from the definition of the gradient. Furthermore, the distance between the heights z_0 and z_1 can be expressed as,

$$z_1 - z_0 = (z_2 - z_0) - (z_2 - z_1) \tag{14}$$

By substituting Eq. (13) into (14), the kinematic condition Eq. (12) can then be recovered. The finite difference form of (12) can be given by,

$$\eta^{n+1}_{i+1/2} = \eta^n_{i+1/2} + \frac{2\Delta t}{\Delta z}\left(\phi^n_{i+1/2,j_s} - \phi^n_{i+1/2,j_s-1/2}\right) - \frac{\Delta t}{2\Delta x^2}\left(\eta^n_{i+3/2} - \eta^n_{i-1/2}\right)F^n_{i+1/2,j_s} \tag{15}$$

where

$$F^n_{i+1/2,j_s} = \frac{1}{2}[T^n_{i+1}(\phi^n_{i+3/2,j_s} - \phi^n_{i+1/2,j_s}) + T^n_i(\phi^n_{i+1/2,j_s} - \phi^n_{i-1/2,j_s})] \tag{16}$$

The subscript j_s denotes the quantity located at the surface and T^n_i is equivalent to the part at LHS of Eq. (11) which represents the rotated effect of the coordinates. It is apparent that the free surface can be traced explicitly with the employment of the quantities, including the horizontal and vertical velocities and the surface slope at last time moment. After the location of surface at the next time level is determined, the potential function at the new site of surface can hence be evaluated by using the dynamic boundary condition. Note that the procedure for locating the interface is exactly the same as that for the surface. Consequently, there is no need to recapitulate it here.

3.3. Moving mesh algorithm

As mentioned earlier, the mesh is treated as moving along with the surface and interface in the vertical direction. When the moving boundaries are displaced to new sites, the computing domain should be re-grided, however, the total grid number keeps unchanged. With $N_{z,u}$ and $N_{z,l}$ representing the total grid numbers of the upper and lower layers in the vertical direction, the unit vertical grid spacing Δz_i^n can then be expressed as,

$$\Delta z_i^n = \begin{cases} \frac{h_1+\eta_i^n-\zeta_i}{N_{z,u}} & \text{for the upper layer} \\ \frac{h_2+\zeta_i^n-H_i}{N_{z,l}} & \text{for the lower layer} \end{cases} \tag{17}$$

where η_i^n, ζ_i^n and H_i represent, in turn, elevations for the surface and interface at the nth time step, and height of the bottom boundary. With Δz_i^n to hand, the vertical coordinate of the cell center $z_{i,j}^n$ can be described by,

$$z_{i,j}^n = \begin{cases} \Delta z_i^n \times j + h_2 & \text{for the upper layer} \\ \Delta z_i^n \times j + H_i & \text{for the lower layer} \end{cases} \tag{18}$$

The above two equations show that the vertical coordinate of each grid is ascertained by the instantaneous locations of the surface and interface. Once the positions of the moving boundaries are determined at the beginning of each time step, the computing area is repartitioned accordingly via solving Eqs. (17) and (18), and the transformation for the spatial differences of the potentials in the domain, Eq. (11), is recalculated.

3.4. Evaluation for the surface potential

To properly evaluate the velocity potential on the moving surface, a relevant expression for the dynamic condition is necessary which is crucial in accounting for the impacts of the boundary's displacement. According to the Lagrangian concept, the formal description of the material derivative for any scalar quantity (including the potential function ϕ) can be expressed as,

$$\frac{\mathrm{d}\phi}{\mathrm{d}t} = \frac{\partial\phi}{\partial t} + \mathbf{U}\cdot\nabla\phi \tag{19}$$

in which $\mathbf{U}$ is the velocity vector. It deserves emphasis that the essential characteristic of this numerical model requires the horizontal coordinate of each grid to keep unchanged during the whole computing period. This means that when dealing with the total time derivative of the potential variables which are frozen horizontally (e.g. $\eta(x_0,t_0)$ and $\eta(x_0,t_1)$ in Fig. 4), one needs to consider only the spatial variation of this quantity in the vertical direction. In other words, the spatial derivative with respect to x should be dismissed from the above Lagrangian expression. Thus, the total time derivative of ϕ should be written as,

$$\frac{\mathrm{d}\phi}{\mathrm{d}t} = \frac{\partial\phi}{\partial t} + v\frac{\partial\phi}{\partial z} = \frac{\partial\phi}{\partial t} + \left(\frac{\partial\phi}{\partial z}\right)^2 \tag{20}$$

Furthermore, the local variation of ϕ with respect to t, $\partial\phi/\partial t$, involved in Eq. (20) can be determined directly from the dynamic boundary condition, i.e.,

$$\frac{\partial\phi}{\partial t} = -\frac{1}{2}|\mathbf{U}|^2 - g\eta = -\frac{1}{2}\left[\left(\frac{\partial\phi}{\partial x}\right)^2 + \left(\frac{\partial\phi}{\partial z}\right)^2\right] - g\eta \tag{21}$$

It is worthy of remark that the term of $\partial\phi/\partial x$ in Eq. (19) represents different physical meaning from those in Eq. (21). The former denotes the spatial variation of the scalar quantity (ϕ) in the horizontal, which vanishes provided this scalar quantity has not been displaced horizontally. Differently, the latter in Eq. (21) represents the local horizontal component of the velocity vector, which is effective for both the Eulerian and the Lagrangian concepts. Thus, this term can not be discarded from Eq. (21) even for a fixed position. Substituting Eq. (21) into (20) yields the practical dynamic condition for the potential variables on the moving surface,

$$\frac{\mathrm{d}\phi}{\mathrm{d}t} = \frac{1}{2}\left[\left(\frac{\partial\phi}{\partial z}\right)^2 - \left(\frac{\partial\phi}{\partial x}\right)^2\right] - g\eta \tag{22}$$

The corresponding difference equation is,

$$\phi^{n+1}_{i+1/2,j_s} = \phi^{n}_{i+1/2,j_s} + \frac{2\Delta t}{\Delta z^2}\left(\phi^{n}_{i+1/2,j_s} - \phi^{n}_{i+1/2,j_s-1/2}\right)^2 - \frac{\Delta t}{2\Delta x^2}\left(F^{n}_{i+1/2,j_s}\right)^2 - \Delta t \cdot g\eta^{n}_{i+1/2} \tag{23}$$

Obviously, in each Lagrangian time interval, the surface potentials at the new position $z_1 = \eta(x_0, t_1)$ can be described explicitly in terms of the variables at the original position $z_0 = \eta(x_0, t_0)$.

3.5. Algorithm for the interfacial conditions

The velocity potentials on the interface can not be determined directly as those on the surface, but need to be evaluated simultaneously with the inner potential variables through solving a large sparse linear system. There are two conditions for relating the potential variables on the two sides of the interface with the inner potentials, one of which is the continuity of normal velocity across the interface:

$$\left[\frac{\partial\phi}{\partial z}\right]_{\zeta+} - \frac{\partial\zeta}{\partial x}\left[\frac{\partial\phi}{\partial x}\right]_{\zeta+} = \left[\frac{\partial\phi}{\partial z}\right]_{\zeta-} - \frac{\partial\zeta}{\partial x}\left[\frac{\partial\phi}{\partial x}\right]_{\zeta-} \tag{24}$$

here subscripts $\zeta+$ and $\zeta-$ stand for the variables at the upper and lower sides of the interface, respectively. Then, the first equation in the discrete form for solving the interfacial potentials can be expressed as,

$$\phi_{i+1/2,j_i+3/2} - \phi_{i+1/2,j_i+1} - \phi_{i+1/2,j_i} + \phi_{i+1/2,j_i-1/2} = \frac{\Delta z}{4\Delta x^2}(\zeta_{i+3/2} - \zeta_{i-1/2})(F_{i+1/2,j_i+1} - F_{i+1/2,j_i}) \tag{25}$$

where the subscript j_i and j_i+1 represent the quantities situated at the lower and upper sides of the interface, respectively. On the other hand, similar as Eq. (20), the material derivatives of the velocity potentials in the z-direction at the two sides of the interface can be given by,

$$\left[\frac{\mathrm{d}\phi}{\mathrm{d}t}\right]_{\zeta+} = \left[\frac{\partial\phi}{\partial t}\right]_{\zeta+} + \left[\left(\frac{\partial\phi}{\partial z}\right)^2\right]_{\zeta+}, \quad \left[\frac{\mathrm{d}\phi}{\mathrm{d}t}\right]_{\zeta-} = \left[\frac{\partial\phi}{\partial t}\right]_{\zeta-} + \left[\left(\frac{\partial\phi}{\partial z}\right)^2\right]_{\zeta-} \tag{26}$$

Furthermore, making use of Eqs. (6) and (7) gives the following dynamic boundary condition on the interface:

$$\left[\frac{\partial\phi}{\partial t}\right]_{\zeta+} - \left[\frac{\partial\phi}{\partial t}\right]_{\zeta-} = \frac{1}{2}\left\{\left[\left(\frac{\partial\phi}{\partial x}\right)^2\right]_{\zeta-} + \left[\left(\frac{\partial\phi}{\partial z}\right)^2\right]_{\zeta-} - \left[\left(\frac{\partial\phi}{\partial x}\right)^2\right]_{\zeta+} - \left[\left(\frac{\partial\phi}{\partial z}\right)^2\right]_{\zeta+}\right\} + \sigma g\zeta \tag{27}$$

By eliminating $[\partial\phi/\partial t]_{\zeta+}$ and $[\partial\phi/\partial t]_{\zeta-}$ from Eqs. (26) and (27), the second equation describing the relationship between the interfacial potentials on the two sides of interface can be rendered as,

$$\left[\frac{\mathrm{d}\phi}{\mathrm{d}t}\right]_{\zeta+} - \left[\frac{\mathrm{d}\phi}{\mathrm{d}t}\right]_{\zeta-} = \frac{1}{2}\left\{\left[\left(\frac{\partial\phi}{\partial x}\right)^2\right]_{\zeta-} - \left[\left(\frac{\partial\phi}{\partial z}\right)^2\right]_{\zeta-} - \left[\left(\frac{\partial\phi}{\partial x}\right)^2\right]_{\zeta+} + \left[\left(\frac{\partial\phi}{\partial z}\right)^2\right]_{\zeta+}\right\} + \sigma g\zeta \tag{28}$$

with the following discrete form,

$$\begin{aligned}\phi^{n+1}_{i+1/2,j_i+1} - \phi^{n+1}_{i+1/2,j_i} = {} & \phi^{n}_{i+1/2,j_i+1} - \phi^{n}_{i+1/2,j_i} + \Delta t \cdot \sigma g\zeta^{n}_{i+1/2} + \tfrac{\Delta t}{2\Delta x^2}\left[\left(F^{n}_{i+1/2,j_i}\right)^2 - \left(F^{n}_{i+1/2,j_i+1}\right)^2\right] \\ & + \tfrac{2\Delta t}{\Delta z^2}\left[\left(\phi^{n}_{i+1/2,j_i+3/2} - \phi^{n}_{i+1/2,j_i+1}\right)^2 - \left(\phi^{n}_{i+1/2,j_i} - \phi^{n}_{i+1/2,j_i-1/2}\right)^2\right]\end{aligned} \tag{29}$$

By coupling Eqs. (25) and (29) with Eq. (10), the unknown potential variables on the two sides of the interface can then be evaluated simultaneously with those in the interior of the domain.

3.6. The lateral boundary conditions

At the two lateral sides of the computing area the non-reflecting boundary condition is needed to prevent the waves from reflecting from the boundary into the domain. A Sommerfeld condition [18] is very appropriate in this case, given by,

$$\left[\frac{\partial\phi}{\partial t}\right]_l + C\left[\frac{\partial\phi}{\partial x}\right]_l = 0 \tag{30}$$

where subscript l denotes the quantities at the lateral boundaries. C represents the wave celerity of an incoming wave. For the sake of simplicity, the random wave speed C is replaced by the linear wave speed C_0,

$$C_0 = \sqrt{\frac{\sigma g h_1 h_2}{h_1 + h_2}} \tag{31}$$

Note that to calculate the potentials at the lateral boundary for the next time step, the material derivative of the potential in the vertical direction Eq. (20) is still useful. By combining Eq. (30) with (20), expression for calculating the potential at the lateral boundary after one time step can be formulated as,

$$\left[\frac{\mathrm{d}\phi}{\mathrm{d}t}\right]_l = \left[\left(\frac{\partial\phi}{\partial z}\right)^2\right]_l - C_0\left[\frac{\partial\phi}{\partial x}\right]_l \tag{32}$$

or written in the discrete form as,

$$[\phi]_{l,t_1} = [\phi]_{l,t_0} + \Delta t\left[\left(\frac{\partial\phi}{\partial z}\right)^2\right]_{l,t_0} - C_0\Delta t\left[\frac{\partial\phi}{\partial x}\right]_{l,t_0} \tag{33}$$

Clearly, the above implementations are applicable only if the linear waves are taken into accounts. As a matter of fact, the nonlinear waves occur more frequently than the linear waves, therefore a damping zone should be added at the end of the domain to eliminate the effects of strong nonlinearity. Such a damping zone, as introduced by, e.g. [19] is a very effective and robust method for preventing wave reflections from the domain boundaries.

In general, the computational procedure for tracking the moving boundaries can be summarized as follows. Firstly, we use the initial values, including the potentials in the interior and those at the boundaries together with locations of the moving boundaries, to evaluate the potentials at the next time step. When all of the potentials and their vertical component of fluxes at the moving boundaries are determined, the new sites of the moving boundaries can then be derived from the kinematic condition. By proceeding iteratively with the above routings, one can thus acquire the integral time series of the sites of the moving boundaries.

3.7. Stability of the method

As is clear previously, the boundary potentials are worked out in an explicit manner which is potentially more convenient for implementation than the implicit method. On the other hand, this does, however, necessitate us finding a stability restriction to avoid the occurrence of the instability and ensure the computation uninterruptedly. Practically, in the case of fixed grids the stability for the equation containing the time derivative term and convective term is given by the CFL-restriction, which in one-dimension reads

$$\frac{\Delta t}{\Delta x}\left|\frac{\partial\phi}{\partial x}\right| \leqslant 1 \tag{34}$$

Although the mesh system of this model is not fixed but moves vertically with the moving boundaries, the CFL condition may still be of relevance for making a criterion for the temporal scales due to the grids are fixed horizontally. According to the wave theory, the stability condition for a progressing wave that prohibits the occurrence of wave breaking is the flow velocity, $|\partial\phi/\partial x|$, less than the wave celerity, C. Furthermore, it is easy to deduce that the probable maximum wave celerity in a two-layer fluid system can be described by the maximum nonlinear speed of the surface wave, that is,

$$C_m = \frac{3}{2}\sqrt{g(h_1 + h_2)} \tag{35}$$

Therefore, the criterion for the time step can be given by,

$$\Delta t \leqslant \frac{\Delta x}{C_m} = \frac{2\Delta x}{3\sqrt{g(h_1 + h_2)}} \tag{36}$$

For instance, considering a two-layer fluid system with total depth 1000 m, if the horizontal spatial scale of a unit grid is set as 150 m, the upper limit for the time step is hence 1 s.

4. Numerical results

For the purpose of demonstrating the effectiveness of this numerical method, two fundamental problems for the interfacial wave dynamics, the generation and evolution of the interfacial waves, are studied. Firstly, the interfacial wave generations by the interplay between the barotropic tide and topography are studied both analytically (see Appendix A) and numerically, and good agreement between the two methods is found. For the next problem, the nonlinear interfacial wave evolutions at various water depth ratios are modeled, and the numerical results are compared favorably with the existing weakly and strongly nonlinear interfacial wave theories.

4.1. Simulations for the interfacial wave generations

As a first step, the generation processes of interfacial waves are simulated and the numerical results are compared with the analytic results obtained in Appendix A. For a weak Gaussian topography, the environmental parameters are outlined as follows: $\sigma = 0.003$, $h_1(h_2) = 100$ m (100 m), $U_0 = 0.1$ ms^{-1}, and $T = 3$ h (here T is the tide period). Additionally, the max height and characteristic horizontal scale of the topography are set as $H_0 = 10$ m and $b = 2000$ m, respectively.

Fig. 5 gives an example of the generation process of the interfacial wave, where the linear features are predominant. It is evident that during each tidal period T, one entire wavelength of interfacial wave is generated and propagates outside from the source position. To make quantitative verifications for the numerical results, more simulations are performed under various topographic and tidal conditions, and the results are compared with the analytical predictions. Fig. 6a plots the dependencies of Λ on F_r, where excellent agreement between the two kinds of results is clear for $\varepsilon = 0.05$. As ε rises to 0.15, a certain discrepancy emerges, likely for the analytical model has limited applications for strong topographies.

Fig. 6b shows a plot of Λ versus δ_b for period $T = 3$ and 12 h, where two remarks can be raised. First, it is apparent that the simulated wave height Λ exhibit reasonable agreement with the analytical results. Second, the simulated value of the critical topographic length b_c is found to be 2.95 (11.79) km as $T = 3$ (12) h, which is exactly identical to that predicted by the analytical formulation $b_c = \sqrt{2}C_0/\omega_0$ (see Appendix A).

In order to manifest this numerical model capable of dealing with the generation of strongly nonlinear interfacial waves, a case of smaller depth ratio and stronger topography is examined. The history of the

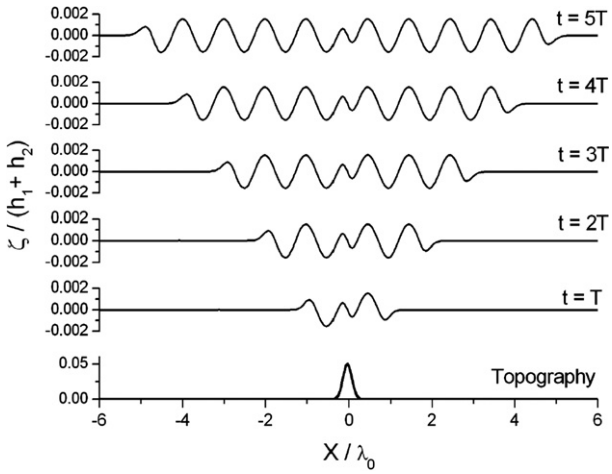

Fig. 5. An example of the interfacial wave generation induced by tidal flow over a Gaussian topography. The normalized topographic height is $\varepsilon = H_0/(h_1 + h_2) = 0.05$, the dimensionless thickness of the upper layer $\delta_h = h_1/(h_1 + h_2) = 0.5$, the Froude number $Fr = U_0/C_0 = 0.0825$, and the tidal period $T = 3$ h. $\lambda_0 = C_0T$ is the wave length of the linear interfacial wave. C_0 is calculated from Eq. (31).

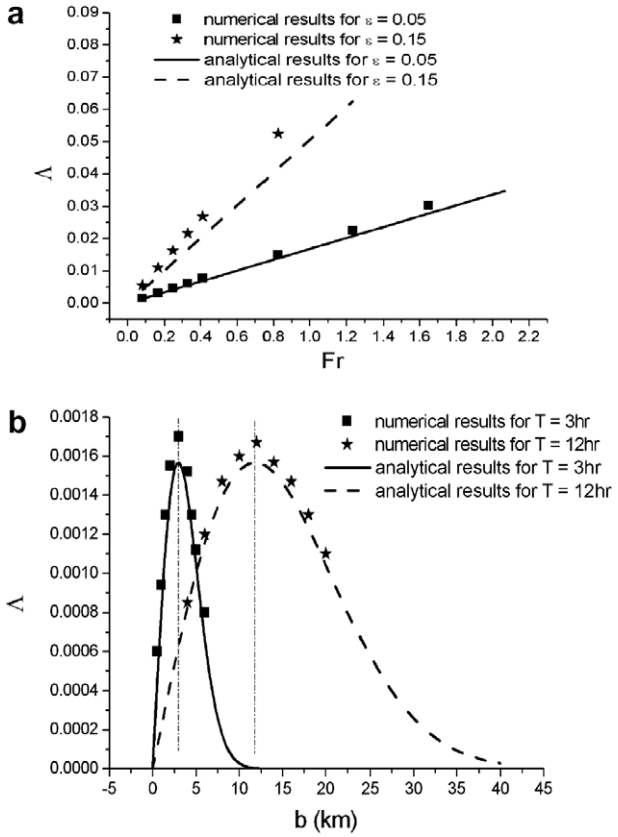

Fig. 6. The dimensionless wave height Λ versus the Froude number Fr (a), and horizontal topographic length b (b). Comparison between the numerical and analytical results.

interfacial displacement is depicted in Fig. 7, where the depth ratio, relative topography magnitude and Froude number are, $\delta_h = 0.1$, $\varepsilon = 0.8$, $F_r = 0.307$, respectively. As seen from Fig. 7, weak undulances are initially created over the sill and then evolve into a train of solitary waves as the tidal flow slackened and turned, which coincides with the observations provided by many researchers [20,21].

It has been demonstrated in Appendix A that resonance effects may arise from the wavelike topographies provided the wavenumber of the topography and the interfacial wave are identical. Here, simulations are performed (Fig. 8) to substantiate this conclusion. A tide of period $T = 1$ h is considered, such that the theoretical wavelength of the interfacial wave is 4365 m according to the known formula for the linear interfacial wave in a two-layer fluid. To identify the resonance effect series of truncated sinusoidal topographies ($\varepsilon = 0.025$) with different wavenumbers are selected. The reason for choosing the truncated sine topographies is to avoid the numerical instability near the lateral boundaries caused by the resonance effect. For the sake of clarity, only two examples are pictured to evidence the resonance effect, in which the wavenumbers of the topographies are 2000 m and 4000 m, respectively, as shown in Fig. 8a and b. Obviously, the interfacial wave generated in Fig. 8b, where wavelength of the topography (4000 m) close to that of the interfacial wave, exhibits intensive magnitude in contrast with the weak example illustrated in Fig. 8a. This shows unambiguously that the resonance effect has emerged even for a truncated topography as long as the wavenumber close to the inherent value of the interfacial wave.

4.2. Simulations for the interfacial wave evolutions

In this section, we would like to get some perspectives on the interfacial wave evolutions. One way of illustrating the usefulness of the current fully nonlinear numerical model is to compare solitary wave solutions with

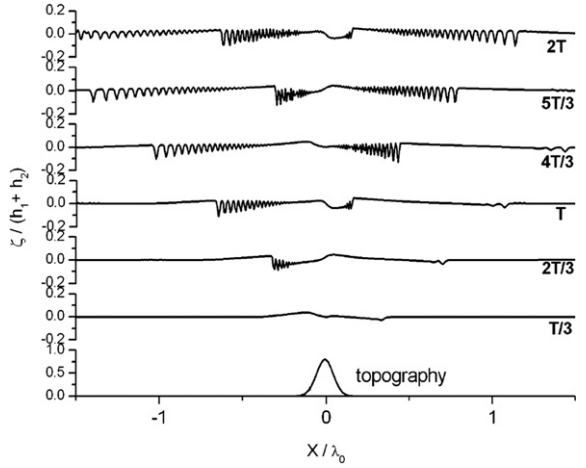

Fig. 7. An example of the generation process of the interfacial solitary waves. The normalized topographic height is $\varepsilon = H_0/(h_1 + h_2) = 0.8$, the dimensionless thickness of the upper layer $\delta_h = h_1/(h_1 + h_2) = 0.1$, the Froude number $Fr = U_0/C_0 = 0.307$, and the tidal period $T = 12$ h.

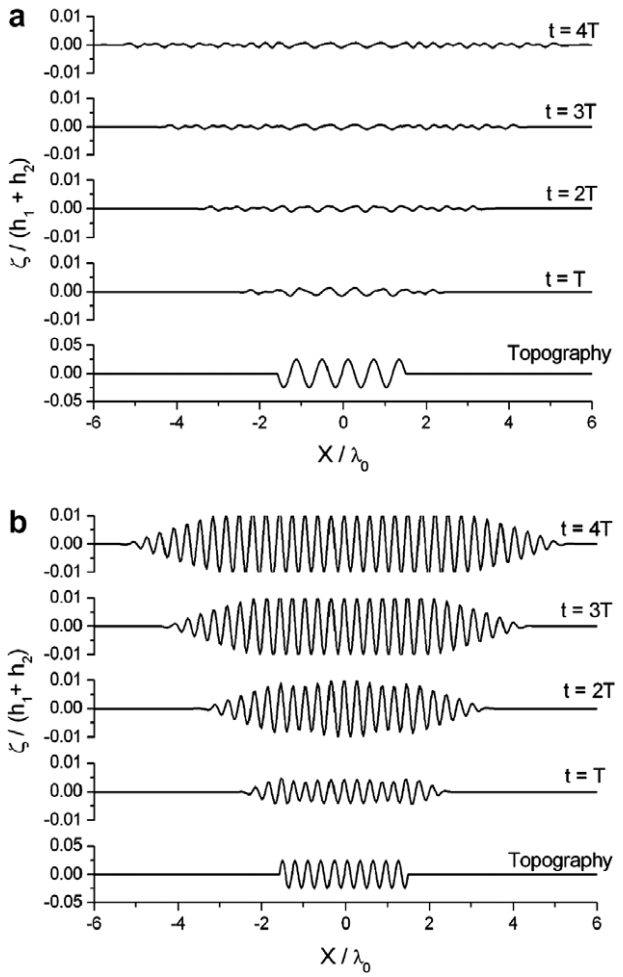

Fig. 8. The generation processes of interfacial waves induced by tidal flows over truncated sinusoidal topographies. The horizontal topographic length scales are 2000 m (a), and 4000 m (b). The water depths $h_1 = h_2 = 100$ m, and the interfacial wave length $\lambda_0 = 4365$ m.

available results by asymptotic theories for such waves, i.e., the KdV theory and the eKdV theory, as mentioned in Section 1. The solitary wave solution for an elevation with amplitude A_0, which is the case when $h_1 > h_2$, may be found in (see e.g. [14]; and the references therein):

$$\zeta(x - Ct) = \frac{A_0}{a + (1-a)\cosh^2[(x-Ct)/\lambda]} \tag{37}$$

$$C = C_0 + \frac{\alpha_1}{3}A_0 + \frac{\alpha_2}{6}A_0^2 \tag{38}$$

$$\lambda^2 = \frac{12\beta}{\alpha_1 A_0 + \frac{1}{2}\alpha_2 A_0^2} \tag{39}$$

$$a = \frac{-\alpha_2 A_0}{2\alpha_1 + \alpha_2 A_0} \tag{40}$$

Here C_0 is the linear phase speed. The coefficients α_1, α_2 and β describe the quadratic and cubic nonlinearities and the dispersion, respectively. For a two-layer system with a rigid lid and no mean flow, in the Boussinesq approximation,

$$\alpha_1 = \frac{3}{2}C_0\frac{h_1 - h_2}{h_1 h_2} \tag{41}$$

$$\alpha_2 = \frac{3C_0}{(h_1 h_2)^2}\left[\frac{7}{8}(h_1 - h_2)^2 - \left(\frac{h_1^3 + h_2^3}{h_1 + h_2}\right)\right] \tag{42}$$

$$\beta = \frac{C_0}{6}h_1 h_2 \tag{43}$$

Note that when α_2 reduces to zero the classical sech^2 solution of the KdV equation is recovered from Eqs. (37)–(40).

Fig. 9 present three cases illustrating evolution process of an initially truncated sinusoidal interfacial wave in various water depth ratiosh_1/h_2, which are 2, 0.5 and 1, respectively, in (a), (b) and (c). The normalized initial wave amplitudes $A_0/(h_1 + h_2)$ are 1/15 (a), 1/15 (b) and 0.05 (c). As seen clearly in Fig. 9a, the frontal part of this harmonic wave becomes narrower with increasing the wave height, until the nonlinearity is balanced by the dispersion effect and ultimately a soliton-like wave is shaped. As is well known from the KdV theory the polarity of a solitary wave is largely dependent on the quadratic nonlinear coefficient α_1: $\alpha_1 > 0$ corresponds to a solitary wave of elevation, and $\alpha_1 < 0$ to one of depression. By invoking Eq. (41) one finds that in this case α_1 is positive for h_1/h_2 greater than unit. Thus, the simulated solitary wave profile exhibiting upward polarity agrees well with the KdV theory. Similarly, one solitary wave of depression is clearly seen in Fig. 9b, as a result of the negative α_1.

In Fig. 9c, the water depth ratio h_1/h_2 equals 1, and, as a result, α_1 reduces to zero, leading to the interfacial wave keeps almost in harmonic. The persistence of an approximately harmonic state can be accounted, in principle, for the fact that the incident wave is substantially weak, that is, the subtle higher nonlinearity is insufficient to have a pronounced effect on the appearance of the wave profile. When the normalized initial wave amplitude exceeds 0.15 as discussed in the latter context, a very distinctive wave configuration may be shaped due to the increased effect of the higher nonlinearity. In general, the simulated wave configurations showing strong dependence on the water depth ratios have provided a striking agreement with the KdV theory.

For more solitary wave solutions the wave profiles are plotted in Fig. 10 and compared with the KdV and eKdV theories, where the fundamental differences between the fully nonlinear and weakly nonlinear models are illustrated. For a weak normalized wave amplitude, $A_0/(h_1+h_2) = 0.05$, the KdV, eKdV and fully nonlinear models are in approximate agreement, as shown in Fig. 10d. However, significant discrepancies between the three solutions emerge for relatively larger wave amplitude. Both of the weakly nonlinear methods underestimate the wave width until $A_0/(h_1 + h_2)$ up to 0.22 (Fig. 10b), where the eKdV solution agrees remarkably well with the fully nonlinear solution. When $A_0/(h_1 + h_2)$ exceeds 0.22 (Fig. 10a) the eKdV solution overestimates the wave width while the KdV solution still maintains a quite small wave width. This variation of

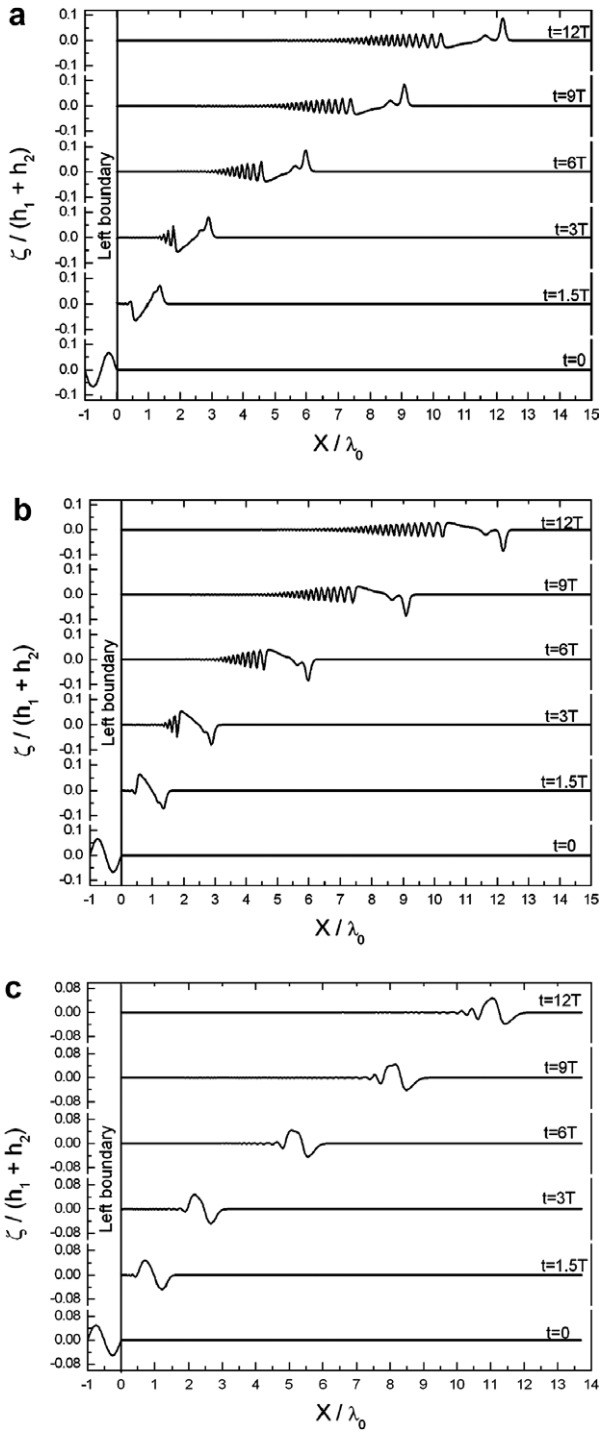

Fig. 9. Examples for the evolution processes of initially truncated sinusoidal interfacial waves. The water depth ratio h_1/h_2 is 2 (a), 0.5 (b) and 1 (c). The normalized initial wave amplitudes $A_0/(h_1 + h_2) = 1/15$, 1/15 and 0.05, respectively, in (a), (b) and (c).

differences of wave widths between the weakly and fully nonlinear solutions depicted in Figs. 10 shows a notable agreement with that made by Helfrich and Melville (see [14, Fig. 5]).

Next, phase speeds for the solitons are measured and compared with the weakly and strongly nonlinear theories. As previously, the phase speed of a solitary wave estimated by the eKdV theory is known to satisfy

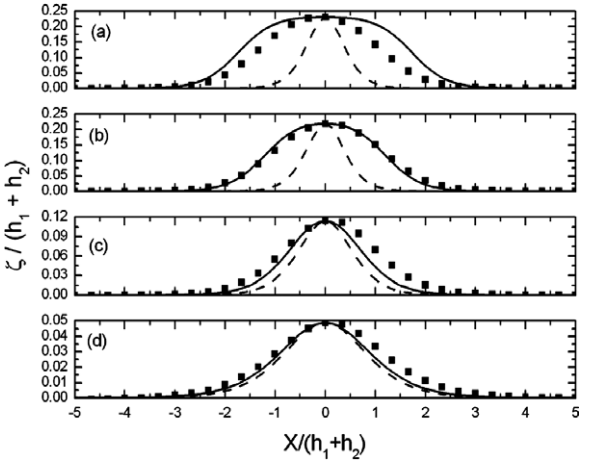

Fig. 10. Profiles of the solitary waves obtained by the numerical model (filled squares), eKdV (solid line) and KdV (dashed line) theories. $h_1/h_2 = 4$ in all cases. The normalized initial wave amplitude, $A_0/(h_1 + h_2)$, = 0.23 (a), 0.22 (b), 0.11 (c), and 0.05 (d).

Eq. (38). In addition, the phase speed for strongly nonlinear interfacial wave has also been derived [15,16], given by (in the Boussinesq limit):

$$V = \sqrt{\frac{\sigma g(h_1 - A)(h_2 + A)}{h_1 + h_2}} \tag{44}$$

Comparisons of the solitary wave speeds between the solutions obtained from the KdV, eKdV, strongly nonlinear (CC) theories and this numerical model are presented in Fig. 11. In Fig. 11a where the depth ratio $h_1/h_2 = 4$, the simulated wave speeds agree well with the CC solutions, and also close to the eKdV solutions but differ notably with the KdV solutions. In Fig. 11b, the depth ratio $h_1/h_2 = 2$ and the results between the simulations, CC solutions and eKdV solutions are indistinguishable. Helfrich and Melville have suggested that the eKdV theory and the fully nonlinear theory agree quite well for $0.4 < h_1/(h_1 + h_2) < 0.6$ and differences grow outside this range (see [14]). Note that the depth ratio $h_1/(h_1 + h_2)$ in Fig. 11b exceeds the aforementioned upper limit to a small extent, but, however, the eKdV and fully nonlinear theories are still in striking agreement.

As mentioned in Section 1 the wave shape of 'thick' solitary wave can not be delineated by the KdV solution, but can be captured by eKdV and strongly nonlinear theories. According to the eKdV theory, as the upper limit ($a \to 1$) is approached the wave begins to broaden until the maximum wave amplitude $A_{0\max} = -\alpha_1/\alpha_2$ is reached. However, a different maximum wave amplitude is produced by the strongly nonlinear (i.e. CC) theory, which is $A_{0\max} = (h_1 - h_2)/2$. Thus, it is of interest to compare the maximum wave amplitudes between the eKdV theory, CC theory, and this fully nonlinear model. The evolution of an initial solitary wave with normalized amplitudes $2A_0/(h_1 - h_2) = 16/9$ is displayed in Fig. 12, where the water depth ratio is $h_1/h_2 = 4$. (At this water depth ratio, the maximum wave amplitudes suggested by the eKdV and CC theories, are $48h_2/41$ and $3h_2/2$, respectively.) One can find clearly from Fig. 12 that the wave decreases its amplitude rapidly at the initial stage and eventually develops a flat-crested wave shape with a maximum wave amplitude, $A_{0\max} = (h_1 - h_2)/2$, precisely the same as that suggested by the CC theory.

Furthermore, it has been stressed in Section 1 that in keeping with the existing asymptotic theories no steady solitary waves can exist in a system at the critical depth ratio. Also, characteristics of the transient interfacial waves at such a depth ratio are still unclear so far. As a consequence, it seems of special interest to give a preliminary elucidation for the wave properties at the critical depth ratio with the employment of the current fully nonlinear method. Fig. 13 presents an example of evolution process of an initially truncated sinusoidal interfacial wave where the normalized initial wave amplitude $A_0/(h_1 + h_2) = 0.2$ and the water depth ratio $h_1/h_2 = 1$. It is clear that the leading half part of the incident wave broadens with decreasing amplitude, as does the rear half. However, there are some differences. Unlike the leading half, the latter grows into a nearly flat-

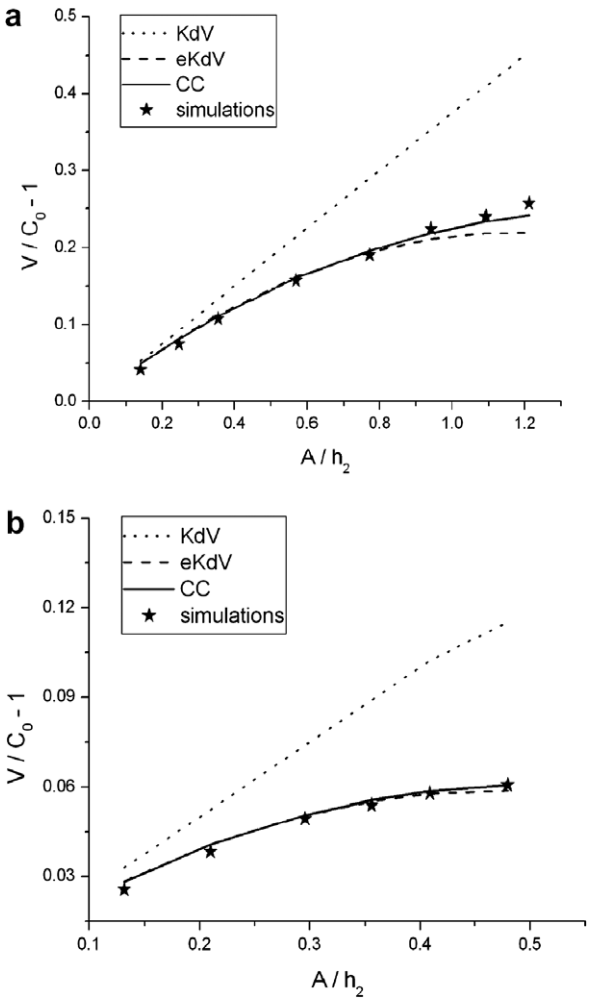

Fig. 11. Soliton speeds normalized by the linear rate: Comparison between the KdV theory (dotted line), eKdV theory (dashed line), CC theory (solid line), and the simulations (stars). The depths ratio $h_1/h_2 = 4$ (a) and 2 (b).

crested wave shape. At the wave crest short solitary waves emerge at the outset and ultimately vanish, which propagate with slower speeds relative to the long wave.

In order to more closely examine the wave properties, the simulated wave profiles are compared for various initial wave amplitudes and the comparisons are displayed in Fig. 14. It is evident in Fig. 14a that the three waves have precisely a same wave length at the initial stage, whilst the wave amplitudes are different. Fig. 14b shows unambiguously that all of these waves become wider with reduced amplitudes contrasting strikingly with their initial states. In particular, one can notice that the waves of greater amplitudes have slower speeds and all less then the linear rate. This is in a sharp contrast with those illustrated in Fig. 11, where the nonlinear phase speed is evidently greater than the linear rate. This result may be partially inferred from Eq. (38), though which is derived from the weakly nonlinear theory. One can readily recognize from this equation that the wave speed C decreases with the wave amplitude A_0 and less than C_0 only if $\alpha_1 = 0$ (note $\alpha_2 < 0$). Likewise, a similar result can be deduced as well from the equation for the wave celerity of strongly nonlinearity, Eq. (44). In general, the above superficial discussion shows that the transient wave properties at the critical depth ratio differ remarkably from the fundamental characteristics of the nonlinear interfacial waves at the non-critical depth ratios. The dispersive effect plays a primary role in the evolution of transient interfacial waves in contrast with the minor effect of the nonlinearity, both tending to reduce the nonlinear wave speed.

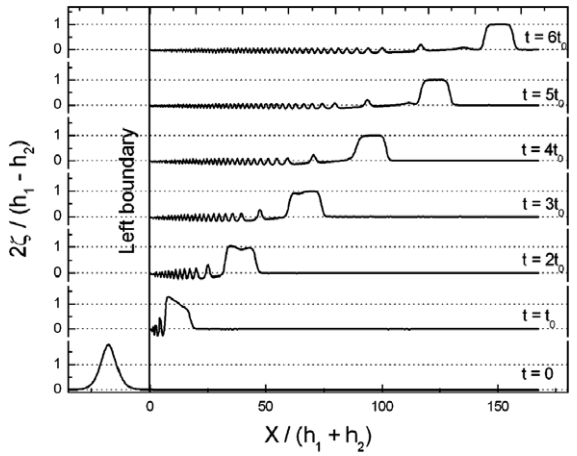

Fig. 12. An example for the evolution process of an initial interfacial solitary wave in a two-layer system ($h_1/h_2 = 4$). The normalized initial wave amplitude $2A_0/(h_1\text{-}h_2) = 16/9$. $t_0(g/h_2)^{1/2} = 1594$.

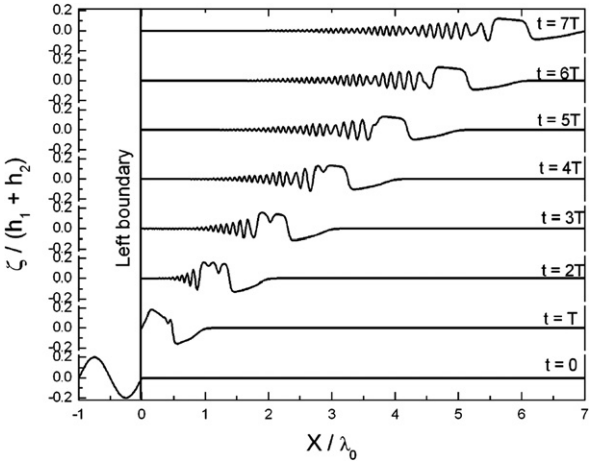

Fig. 13. An example for the evolution process of an initially truncated sinusoidal interfacial wave in a two-layer system ($h_1/h_2 = 1$). The normalized initial wave amplitude $A_0/(h_1 + h_2) = 0.2$, the normalized period $T(g/h_2)^{1/2} = 1594$, and λ_0 is the wavelength of the linear interfacial wave.

4.3. Convergence results

To check the numerical convergence of the method, simulations have been performed for the generation and evolution of the interfacial waves under different grid points. Firstly, interfacial wave generations over weak topography are considered. The environmental data are the same as those of Fig. 5. For grid refinement, four different grids have been used with 400×40, 200×40, 100×20 and 70×20 grid points. The results are compared with the analytical result (Eq. (A.17)) and presented in Fig. 15a. Table 1 shows the maximum errors for the wave height and wave length relative to the analytical results. It is clear from the plot and table that the numerical method is convergent with increasing the resolution. Furthermore, the evolutions of an initial soliton for four different grids are performed where the environmental data are akin to those of case (b) in Fig. 10. The results are compared with the eKdV theory (Fig. 15b) and the maximum errors for the wave height are provided (the wave length of a soliton is infinite which is hence not measured), from which as well the convergence of the numerical method is apparent.

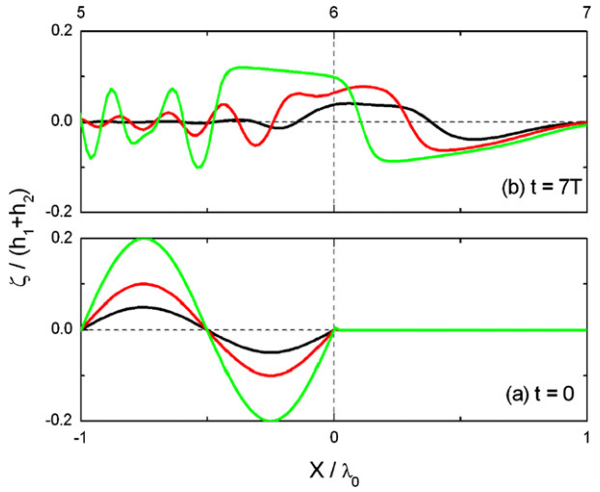

Fig. 14. Wave profiles at time $t = 0$ (a) and $7T$ (b): Comparisons between various initial wave amplitudes. The normalized initial wave amplitude $A_0/(h_1 + h_2) = 0.05$ (black line), 0.1 (red line), and 0.2 (green line). (For interpretation of the references in colour in this figure legend, the reader is referred to the web version of this article.)

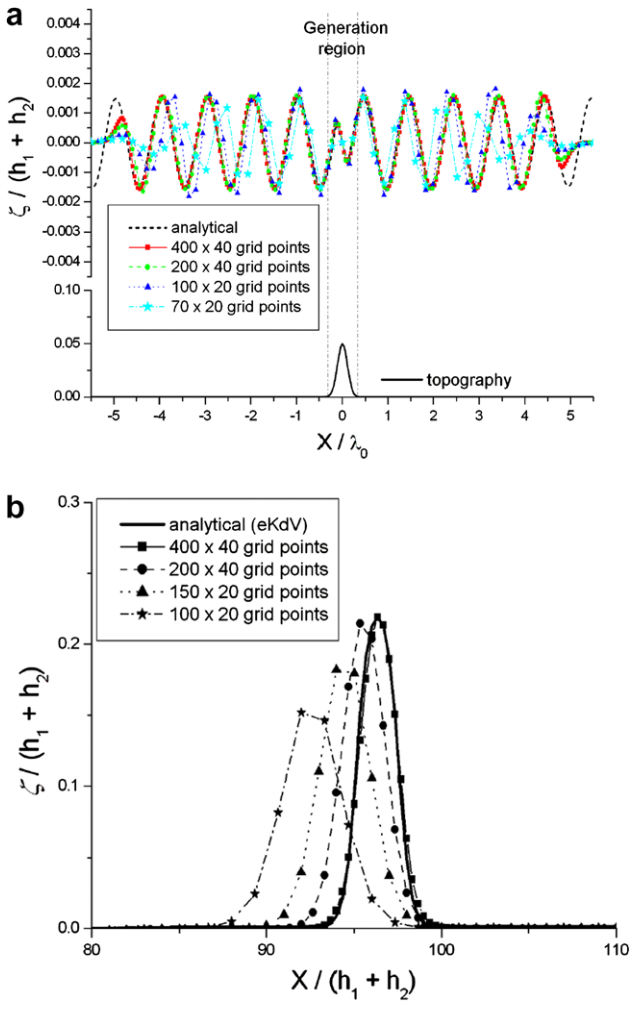

Fig. 15. Convergence of the method. Generation of the linear waves (a), evolution of the solitons (b).

Table 1
Normalized maximum errors in wave height (W_h) and wave length (W_l) with different resolutions for the plots in Fig. 15a and b.

	Grid points	70×20	100×20	200×40	400×40
Generations	W_h-errors	0.73	0.4	0.093	0.047
	W_l-errors	0.15	0.09	0.004	0.008
Evolutions	W_h-errors	0.31	0.17	0.02	0.0004

5. Conclusions

A fully nonlinear and dispersive numerical model for interfacial waves in two-layer systems was proposed by employing an efficient 'front-tracking' method. The essential technique, taking full advantages of the Eulerian and Lagrangian concepts, was fulfilled by adjusting vertical scales of the mesh system along with the instantaneous sites of the moving boundaries but keeping the horizontal coordinates of each grids unchanged. In such a moving mesh system, a modified dynamic boundary condition thus became indispensable for the accurate evaluation of the boundary potentials.

Two important processes of interfacial wave dynamics were simulated to validate the reliability and accuracy of this numerical method. Firstly, in consideration of the interfacial wave generation the simulated wave characteristics showed good agreement with the analytic predictions. Further, the interfacial solitary wave evolutions were modeled in various water depth ratios, aiming at demonstrating the capability of simulating strongly nonlinear interfacial waves as well as revealing the prominent features of those at the critical depth ratio. In reproducing the nonlinear interfacial solitary waves at the non-critical depth ratios, excellent agreement was exhibited upon comparing the essential wave features with the asymptotic theories. Moreover, the propagation and evolution of internal bores (wave amplitude attained the maximum) were simulated successfully and the resulting wave amplitude agreed perfectly with the fully nonlinear wave theory, which manifested the numerical model more competent than the weakly nonlinear theories. Finally, simulations at the critical depth ratio presented an unusual result different to the common knowledge of the nonlinear waves: the dispersive effect was found to play a more significant role than the nonlinearity and the nonlinear wave speed was decreased to below the linear rate.

Acknowledgement

The author gratefully acknowledges the financial support provided by the National Natural Science Foundation of China under Grant 10602060 and the helpful comments from anonymous reviewers.

Appendix A. Analytical expressions for the surface and interfacial elevations triggered by the forcing sources at the bottom

For an inviscid and incompressible fluid, if assuming the motion in each layer is irrotational, the governing equations can be given by the potential theory as follows:

$$\begin{aligned} &\Delta\phi^{(u)} = 0, \quad -h_1 < z < 0 \\ &\Delta\phi^{(l)} = 0, \quad -(h_1 + h_2) < z < -h_1 \end{aligned} \tag{A.1}$$

where superscripts $^{(u)}$ and $^{(l)}$, henceforth, denotes the quantities of the upper and lower layers, respectively. The linearized boundary conditions on the surface and interface are given by,

$$\begin{aligned} &\begin{cases} \eta_t = \phi_z^{(u)} \\ \phi_t^{(u)} + g\eta = 0 \end{cases}, \quad z = 0 \\ &\begin{cases} \varsigma_t = \phi_z^{(u)} = \phi_z^{(l)} \\ (1-\sigma)[\phi_t^{(u)} + g\varsigma] = \phi_t^{(l)} + g\varsigma \end{cases}, \quad z = -h_1 \end{aligned} \tag{A.2}$$

From the fundamental conception for the long internal wave generation by the tide flow over uneven topography [22], the bottom boundary condition can be written as,

$$\phi_z^{(1)} = U_0 H_x(x)\mathrm{e}^{\mathrm{i}\omega_0 t}, \quad z = -(h_1 + h_2) \tag{A.3}$$

here U_0 and ω_0 represent the velocity and frequency of the barotropic tide current, respectively. In order to obtain the formal solution of this problem, we resort to the Laplace transform with respect to t and the Fourier transform with respect to x defined by,

$$\tilde{\bar{f}}(k,s) = \frac{1}{\sqrt{2\pi}} \int_{-\infty}^{\infty} \mathrm{e}^{-\mathrm{i}kx}\,\mathrm{d}x \int_0^{\infty} \mathrm{e}^{-st} f(x,t)\mathrm{d}t \tag{A.4}$$

where the tilde and bar are used to represent the Fourier and Laplace transformations, respectively. Application of the joint integral transformations gives the integral solutions,

$$\begin{aligned}
\phi^{(\mathrm{u})} &= \tfrac{\mathrm{i}U_0}{\sqrt{2\pi}} \textstyle\int_{-\infty}^{\infty} \frac{\widetilde{H}(k)\mathrm{e}^{\mathrm{i}kx}}{gk} \frac{1}{2\pi\mathrm{i}} \int_{B_\mathrm{r}} \frac{s^2\left(\frac{s^2}{kg}\mathrm{sh}\,kz - chkz\right)\mathrm{e}^{st}}{G(k,s)(s-\mathrm{i}\omega_0)}\mathrm{d}s\,\mathrm{d}k,\\
\phi^{(\mathrm{l})} &= \tfrac{\mathrm{i}U_0}{\sqrt{2\pi}} \textstyle\int_{-\infty}^{\infty} \widetilde{H}(k)\mathrm{e}^{\mathrm{i}kx} \frac{1}{2\pi\mathrm{i}} \int_{B_\mathrm{r}} \frac{-\mathrm{e}^{st}}{G(k,s)(s-\mathrm{i}\omega_0)}\\
&\quad\times\Big\{\Big[\tfrac{s^4}{k^2g^2}(\mathrm{sh}\,k(h_1+h_2) - \sigma\mathrm{sh}\,kh_1 chkh_2) + \tfrac{s^2}{kg}chk(h_1+h_2)\\
&\quad+\sigma\mathrm{sh}\,kh_1 chkh_2]chk(z+h_1+h_2) - G(k,s)\mathrm{sh}\,k(z+h_1+h_2)\Big\}\mathrm{d}s\,\mathrm{d}k
\end{aligned} \tag{A.5}$$

$$\eta = \frac{\mathrm{i}U_0}{\sqrt{2\pi}g^2} \int_{-\infty}^{\infty} \frac{\widetilde{H}(k)\mathrm{e}^{\mathrm{i}kx}}{k} \frac{1}{2\pi\mathrm{i}} \int_{B_\mathrm{r}} \frac{s^3\mathrm{e}^{st}}{G(k,s)(s-\mathrm{i}\omega_0)}\mathrm{d}s\,\mathrm{d}k \tag{A.6}$$

$$\begin{aligned}
\varsigma &= \tfrac{\mathrm{i}U_0}{\sqrt{2\pi}\sigma g} \textstyle\int_{-\infty}^{\infty} \widetilde{H}(k)\mathrm{e}^{\mathrm{i}kx} \frac{1}{2\pi\mathrm{i}} \int_{B_\mathrm{r}} \frac{s\mathrm{e}^{st}}{G(k,s)(s-\mathrm{i}\omega_0)}\\
&\quad\times\left\{\begin{array}{l}
\frac{s^4}{k^2g^2}[(\mathrm{sh}\,k(h_1+h_2) - \sigma\mathrm{sh}\,kh_1 chkh_2)chkh_2 - (1-\sigma)\mathrm{sh}\,kh_1]\\
+\frac{s^2}{kg}[chk(h_1+h_2)chkh_2 - (1-\sigma)chkh_1]\\
+\sigma\mathrm{sh}\,kh_1 chkh_2 chkh_2 - G(k,s)\mathrm{sh}\,kh_2
\end{array}\right\}\mathrm{d}s\,\mathrm{d}k
\end{aligned} \tag{A.7}$$

where,

$$\begin{aligned}
G(k,s) &= \tfrac{R(k)}{k^2g^2}s^4 + \tfrac{\mathrm{sh}\,k(h_1+h_2)}{kg}s^2 + \sigma\mathrm{sh}\,kh_1\mathrm{sh}\,kh_2,\\
R(k) &= chk(h_1+h_2) - \sigma\mathrm{sh}\,kh_1\mathrm{sh}\,kh_2
\end{aligned} \tag{A.8}$$

Evidently, $G(k,s) = 0$ gives the dispersion relation of this problem, roots of which satisfy,

$$s^2 = \frac{kg\mathrm{sh}\,k(h_1+h_2)}{2R(k)} \times \left[-1 \pm \sqrt{1 - \frac{4\sigma R(k)\mathrm{sh}\,kh_1\mathrm{sh}\,kh_2}{\mathrm{sh}^2 k(h_1+h_2)}}\right] \tag{A.9}$$

Note that the above equation exists four pure imaginary roots, which are presumed to be $s_1 = \omega_1(k)\mathrm{i}$, $s_2 = -\omega_1(k)\mathrm{i}$, $s_3 = \omega_2(k)\mathrm{i}$ and $s_4 = -\omega_2(k)\mathrm{i}$, respectively, (herein $\omega_1 > \omega_2 > 0$). Under the shallow water and Boussinesq approximations ($\sigma \ll 1$), we have,

$$\omega_1 = k\sqrt{g(h_1+h_2)}, \quad \omega_2 = k\sqrt{\sigma g\frac{h_1h_2}{h_1+h_2}} \tag{A.10}$$

This is the familiar dispersion relations for the surface and interfacial waves in a two-layer fluid. By applying the Cauchy's residue theorem, together with the shallow water and Boussinesq approximations, the steady state solutions of Eqs. (A6) and (A7) can be acquired as,

$$\eta = \frac{\sqrt{\pi}U_0\omega_0}{\sqrt{2}g(h_1+h_2)} Im\left[-\widetilde{H}(k_1)\mathrm{e}^{\mathrm{i}(\omega_0 t - k_1|x|)} + \widetilde{H}(k_2)\mathrm{e}^{\mathrm{i}(\omega_0 t - k_2|x|)}\right] \tag{A.11}$$

$$\zeta = -\mathrm{sgn}x \cdot \sqrt{\frac{\pi}{2}}\frac{U_0\omega_0}{\sigma g h_2} Im\left[\frac{\sigma h_2^2}{(h_1+h_2)^2}\widetilde{H}(k_1)\mathrm{e}^{\mathrm{i}(\omega_0 t - k_1|x|)} + \widetilde{H}(k_2)\mathrm{e}^{\mathrm{i}(\omega_0 t - k_2|x|)}\right] \tag{A.12}$$

here the wave numbers k_1 and k_2 satisfy,

$$k_1 = \frac{\omega_0}{\sqrt{g(h_1+h_2)}}, \quad k_2 = \omega_0 \Big/ \sqrt{\sigma g \frac{h_1 h_2}{h_1+h_2}} \tag{A.13}$$

Considering a Gaussian topographic profile defined by $H(x) = H_0\exp(-x^2/b^2)$, Eqs. (A11) and (A12) can be rewritten as,

$$\eta = \frac{\sqrt{\pi}U_0\omega_0 H_0 b}{2g(h_1+h_2)}\,\mathrm{Im}\left[-\exp\left(-\frac{b^2k_1^2}{4}\right)e^{i(\omega_0 t - k_1|x|)} + \exp\left(-\frac{b^2k_2^2}{4}\right)e^{i(\omega_0 t - k_2|x|)}\right] \tag{A.14}$$

$$\begin{aligned}\zeta = &-\mathrm{sgn}x \cdot \tfrac{\sqrt{\pi}U_0\omega_0 H_0 b}{2\sigma g h_2}\,\mathrm{Im}\left[\tfrac{h_2^2\sigma}{(h_1+h_2)^2}\exp\left(-\tfrac{b^2k_1^2}{4}\right)e^{i(\omega_0 t - k_1|x|)}\right.\\ &\left.+\exp\left(-\tfrac{b^2k_2^2}{4}\right)e^{i(\omega_0 t - k_2|x|)}\right]\end{aligned} \tag{A.15}$$

As seen from these two equations, both the surface and interfacial elevations comprise two modes of waves, the fast and slow modes, phase speeds of which are ω_0/k_1 and ω_0/k_2, respectively. By comparing wave amplitudes of the two kinds of waves, we can readily identify that amplitude of the interfacial wave of the slow mode is much greater than the other components and hence deserves a detailed examination. By using the following dimensionless variables:

$$\Lambda = \frac{A}{h_1+h_2}, \quad \varepsilon = \frac{H_0}{h_1+h_2}, \quad F_r = \frac{U_0}{C_0}, \quad \delta_h = \frac{h_1}{h_1+h_2}, \quad \delta_b = bk_2 = \frac{b\omega_0}{C_0} \tag{A.16}$$

amplitude of the interfacial wave of the slow mode takes a dimensionless form as,

$$\Lambda = \frac{\sqrt{\pi}}{2}F_r\delta_h\varepsilon\delta_b\exp\left(-\frac{\delta_b^2}{4}\right) \tag{A.17}$$

where C_0 represents the linear phase speed of interfacial wave of the slow mode, Λ the dimensionless wave amplitude, ε the dimensionless topographic height, F_r the Froude number for the ocean tidal current, δ_h the dimensionless thickness of the upper layer, and δ_b is the dimensionless horizontal topographic length. The above equation shows clearly that Λ is a monotonically increasing function of F_r and ε, while takes a maximum as δ_b^2 up to 2, where the corresponding critical value is $b_c = \sqrt{2}C_0/\omega_0$.

In addition, if a bottom feature like a wavelike profile is taken into consideration, it is easy to check that expression for the wave amplitude may tend to infinite provided the wave numbers of the topography and the interfacial wave are equal. In other words, a resonance effect that breaks down the linear theory occurs at this stage.

References

[1] C.W. Hirt, B.D. Nichols, Volume of fluid (VOF) method for dynamics of free boundaries, J. Comput. Phys. 39 (1981) 201–225.
[2] S. Osher, J.A. Sethian, Front propagating with curvature-dependent speed: algorithms based on Hamilton–Jacobi formulations, J. Comput. Phys. 79 (1988) 12–49.
[3] S.O. Unverdi, G. Tryggvason, A front-tracking method for viscous incompressible multi-fluid flows, J. Comput. Phys. 100 (1992) 25–37.
[4] F.S. de Sousa, N. Mangiavacchi, L.G. Nonato, A. Castelo, M.F. Tomé, V.G. Ferreira, J.A. Cuminato, S. McKee, A front-tracking/front-capturing method for the simulation of 3D multi-fluid flows with free surface, J. Comput. Phys. 198 (2004) 469–499.
[5] C.M.P. Silva Santos, D.M. Greaves, A mixed Lagrangian–Eulerian method for non-linear free surface flows using multi-grid on hierarchical Cartesian grids, Comput. Fluids 36 (2007) 914–923.
[6] S. Rabier, M. Medale, Computation of free surface flows with a projection FEM in a moving mesh framework, Comput. Methods Appl. Mech. Eng. 192 (2003) 4703–4721.
[7] T.E. Tezduyar, Interface-tracking and interface-capturing techniques for finite element computation of moving boundaries and interfaces, Comput. Methods Appl. Mech. Eng. 195 (2006) 2983–3000.
[8] T.B. Benjamin, Internal waves of finite amplitude and permanent form, J. Fluid Mech. 25 (1966) 241–270.
[9] T.B. Benjamin, Internal waves of permanent form in fluids of great depth, J. Fluid Mech. 29 (1967) 559–592.
[10] H. Ono, Algebraic solitary waves in stratified fluids, J. Phys. Soc. Jpn. 39 (1975) 1082–1091.
[11] R.I. Joseph, Solitary waves in finite depth fluids, J. Phys. A 10 (1977) L225–L227.
[12] R. Grimshaw, Environmental Stratified Flows, Kluwer, 2002.

[13] P.E. Holloway, E. Pelinovsky, T. Talipova, A generalized Korteweg–de Vries model of internal tide transformation in the coastal zone, J. Geophys. Res. 104 (1999) 18333–18350.
[14] K.R. Helfrich, W.K. Melville, Long nonlinear internal waves, Annu. Rev. Fluid Mech. 38 (2006) 395–425.
[15] W. Choi, R. Camassa, Fully nonlinear internal waves in a two-fluid system, J. Fluid Mech. 396 (1999) 1–36.
[16] L.A. Ostrovsky, J. Grue, Evolution equations for strongly nonlinear internal waves, Phys. Fluids 15 (2003) 2934–2948.
[17] T.C. Jo, W. Choi, Dynamics of strongly nonlinear internal solitary waves in shallow water, Stud. Appl. Math. 109 (2002) 205–227.
[18] I. Orlanski, A simple boundary condition for unbounded hypobolic flows, J. Comput. Phys. 21 (1976) 251–269.
[19] A. Clément, Coupling of two absorbing boundary conditions for 2D time-domian simulations of free surface gravity waves, J. Comput. Phys. 126 (1996) 139–151.
[20] A.R. Osborne, T.L. Burch, Internal solitons in the Andaman Sea, Science 208 (1980) 451–460.
[21] J.R. Apel, H.M. Byrne, J.R. Proni, R.L. Charnell, Observations of oceanic internal and surface waves from the Earth resources technology satellite, J. Geophys. Res. 80 (1975) 865–881.
[22] C. Garrett, E. Kunze, Internal tide generation in deep ocean, Annu. Rev. Fluid Mech. 39 (2007) 57–87.